JOURNAL OF MATERIALS SCIENCE 30 (1995) 1069–1074

NMR characterization of injection-moulded alumina green compacts

Part II T_2-weighted proton imaging

PU SEN WANG, S. G. MALGHAN, S. J. DAPKUNAS
Ceramics Division, Materials Science and Engineering Laboratory, National Institute of Standards and Technology, Gaithersburg, MD 20899, USA

K. F. HENS, R. RAMAN
Department of Engineering Science and Mechanics, Pennsylvania State University, University Park, PA 16802, USA

Injection-moulded alumina green compacts containing polypropylene, wax, and stearic acid were studied for binder distribution by proton nuclear magnetic resonance (^{1}H NMR) imaging. The solid imaging technique of nuclear spin–spin relaxation time, T_2, weighted imaging at 400 MHz was used. This imaging technique utilizes a multiple pulse sequence of D_0–$(\pi/2)_{\pm x}$–τ–D_{10}–D_7–$(\pi)_x$–D_7–D_{10}–AQ–D_0 for echo detection and phase encoding. Two- and three-dimensional images were constructed from the intensities of these nuclear echo signals. Spatially resolved two-dimensional images obtained by the application of this technique indicated that the green compacts fabricated from the same nominal binder composition did not contain the same amounts of binder. This observation agrees well with our previous conclusion drawn from nuclear spin echo studies by Hahn's pulse sequence. A $64 \times 64 \times 64$ three-dimensional imaging revealed that the inhomogeneity of binder distribution and internal imperfection do exist at certain locations of the samples. A binder-rich folding line was also detected in one of these green compacts.

1. Introduction

Injection moulding offers the advantage of fabricating ceramic components of complex shapes with high dimensional accuracy. However, several factors impact on the reproducibility and thus cost in producing components by injection moulding. These factors include powder characteristics [1–4], choice of binder [5, 6], mixing of blends [7–10], moulding parameters [11–13], and binder removal [14]. NMR imaging appears to be one of the techniques suitable to study some of these factors in order to improve reproducibility and decrease production cost.

NMR imaging is a well-established technique for the study of biological systems and for medical diagnosis. The imaging method uses a magnetic field gradient to encode the positions of the nuclear spins with a spatially varying Larmor frequency. Once the variations in resonant frequency have been decoded, an image of NMR parameters can be created. This technique possesses several fundamental advantages over other mapping techniques: (a) the sample can be characterized *in situ* for different nuclei at different frequencies for their spatial distribution; (b) the sample can be characterized *in situ* in a number of ways, e.g. not only spin densities but also different relaxation times can be measured to understand the environment of a specific nuclear spin; (c) any plane can be imaged without actually slicing the sample; (d) the method is non-destructive.

However, the application of NMR imaging to materials diagnosis is challenging because the spatial resolution, δ, in NMR imaging is related to the natural linewidth, ν, and the applied field gradient, G, by

$$\delta = \nu/\gamma G \quad (1)$$

where γ is the gyromagnetic ratio of the nucleus observed. In solids, the linewidth is usually several hundred times broader than in liquids or for the human body, because of the nuclear dipolar interactions. Consequently, the line narrowing technique and a large field gradient are the key factors in solid NMR imaging. Several studies have been published in the literature focusing on NMR imaging of ceramics [15–22]. Most of these studies involve binder distributions in green bodies. We have previously published such a study involving a stray-field NMR imaging technique which utilizes a high gradient planar surface below a 9.394 superconducting magnet resonating at 163 MHz [23]. We have also reported, in Part I, the results of an NMR spin–spin relaxation study on the injection-moulded alumina green compacts [24]. In Part I, we measured ^{1}H nuclear spin echo signals of these compacts and their pure binder components by

0022–2461

a $(\pi/2)$–τ–π–τ pulse sequence at 400 MHz. The nuclear spin–spin relaxation times, T_2, of the pure binder components, paraffin wax, polypropylene, and stearic acid, were calculated by Bloch's equations using the respective echo intensity decay characteristics. A species with T_2 near 300 μs in the green compacts was also observed. Variations in binder content were detected in these compacts which were fabricated from the same nominal blend composition. In this paper, Part II of the study, we present the results for these compacts as characterized by T_2-weighted ^{1}H NMR imaging. The T_2-weighted imaging technique utilizes the characteristic spin–spin relaxation time of the monitoring nucleus to perform imaging. The NMR imaging technique used is based on a gradient-coiled, micro-imaging approach at 400 MHz. Injection-moulded green compacts are an interesting and classical example for NMR imaging because of high binder concentration and multiple binder components which may be resolved for different T_2 mapping.

2. Experimental procedure*

2.1. Injection moulding of green compacts

The feedstock was prepared by mixing Alcoa A-17 alumina powder with a binder. The mixture consisted of 65 vol % alumina and 35 vol % binder. The binder constituents were 62 wt % paraffin wax, 33 wt % polypropylene, and 5 wt % stearic acid. All binder components were in powder form and were blended in a high shear-rate blender with intensifier bar for 10 min at 60 r.p.m. blending bowl speed and 3000 r.p.m. intensifier bar speed. This powder mixture was fed via a vibratory/screw type feeder into a twin-screw processor at 27 $cm^3\,min^{-1}$.

Injection moulding was performed using a feedback-controlled Engel powder injection-moulding machine. This machine is a microprocessor-controlled injection-moulding machine specially equipped to process metal and ceramic powder mixtures. All parts were processed using the same moulding conditions. A nozzle/barrel temperature profile of 105, 110, 110, 97 °C from nozzle through three barrel heating sections was used. The feeding throat of the moulding machine was chilled to 18 °C. The mould temperature was kept constant via a water circulator at 28 °C. Injection was performed at a fixed, feedback-controlled filling speed profile. During filling of sprue and runner system, a screw speed of 6 $cm\,s^{-1}$ was used for the 22 mm diameter screw. Once the melt-front reached the gate, the speed was reduced to 1 $cm\,s^{-1}$ to build up a more viscous melt-front. This is done to avoid "jetting" of the material through the mould resulting in back-filling. Subsequently, the speed was increased to 8.4 $cm\,s^{-1}$ to ensure that the entire fracture bar was filled before the material solidified. The entire filling cycle took 0.3 s. When a piezoelectric quartz cavity pressure transducer sensed 2 MPa in the mould cavity, control was changed over to pressure control for packing. This stage is used to compress the feedstock in the cavity to compensate for shrinkages during cooling and solidification of the compact. A pressure profile ranging from 20–30 MPa was applied to the melt for 2 s. A 15 s cooling cycle was used before the mould was opened and the compact ejected.

All three samples (13 mm × 13 mm × 3.2 mm in dimension) were studied simultaneously in a 20 mm diameter NMR tube so that a comparison can be obtained without any instrumental parameter variation.

2.2. Spectrometer and imaging facility

The NMR imaging facility consists of a Bruker MSL-400 system with a selective excitation unit, a micro-imaging probe, a gradient drive unit, a low power (5 W) linear amplifier, and other accessories. This spectrometer has a superconducting magnet of 9.394 T which corresponds to a ^{1}H resonant frequency of ~400 MHz. Our actual resonant frequency was 400.159 972 ± 0.000 001 MHz. A 20 mm diameter r.f. coil insert was used for detecting the T_2 of binder of the green compacts. The r.f. transmitter generates a pulse which is amplified by the 5 W linear amplifier for a $(\pi/2)$ nuclear flip. The $(\pi/2)$ pulse width of this r.f. coil was 19.5 μs.

The selective excitation unit was designed to generate shaped pulses which will be mixed with the hard r.f. pulse (from the linear amplifier) for frequency-selected excitation. However, because of the short T_2 for solids [24], the shaped pulse was not used. Instead, an incremental phase encoding along the z-axis was utilized for the third dimension excitation. The selective excitation unit also generated pulses for the gradient coils. These pulses were first sent into a pre-emphasis unit for shaping and then fed into the gradient drive unit. The pre-emphasis unit is needed to correct the pulse-shape distortion due to the eddy current when the gradient coils are turned on. The gradient drive unit consists of two audio power amplifiers and a pre-emphasis unit. A set of gradient coils was inserted around the r.f. coil to generate a maximum field gradient of approximately 6×10^{-3} $T\,cm^{-1}$ for phase encoding.

To step up the field gradient in each dimension, 64 increments were applied. The pulse sequence used to acquire echo signals, phase encoding, and T_2-weighting for image construction is D_0–$(\pi/2)_{\pm x}$–τ–D_{10}–D_7– $(\pi)_x$–D_7–D_{10}– AQ–D_0 where τ is the variable delay between the 90° and 180° pulses in Hahn's echo detection sequence [24–26] and also used here for phase encoding time, AQ is the echo acquisition time and D_7 and D_{10} are delays for T_2-weighting and gradient coil stabilization, respectively. D_0 is a long delay (800 ms in our experiments) for the bulk nuclear magnetization vector, M, to relax back to the z-axis through nuclear spin–crystal lattice relaxation and reach the spin temperature equilibrium in preparation for the next experiment.

* Certain commercial equipment, instrument, or materials are identified in this paper in order to specify adequately the experimental procedure. Such identification does not imply recommendation or endorsement by the National Institute of Standards and Technology, nor does it imply that the materials or equipment identified are necessarily the best available for the purpose.

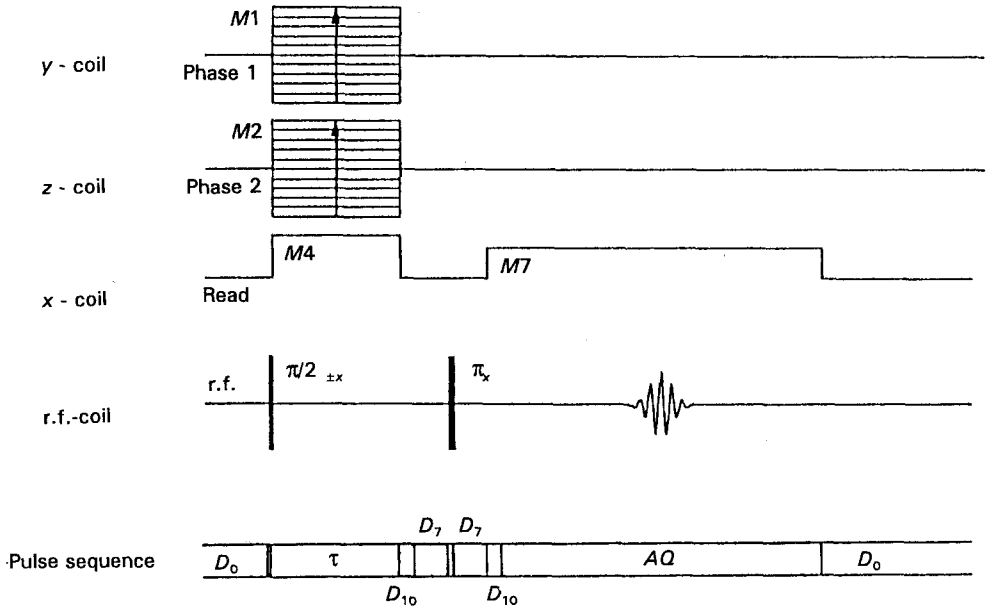

Figure 1 Schematic illustration of the pulse sequence to acquire a phase-encoded T_2-weighted NMR image. The *M*s are field gradient multipliers.

3. Results and discussion

Fig. 1 shows the sequence to acquire a phase encoded, T_2-weighted NMR image. The $M1$, $M2$, and $M4$ in this figure represent the field gradient multipliers of the y-, z-, and x-gradient coil, respectively. In the acquisition of a three-dimensional image, a long delay of 800 ms, D_0, was applied to the sample first. In this period, all power to the r.f. and gradient coils was turned-off so that the nuclei could be relaxed and equilibrated. Then, the sample was irradiated with a $(\pi/2)_x$ r.f. pulse by the transmitter to turn the nuclear magnetization vector, M, from the z- to the y-axis. At the end of this 90° pulse, a variable delay, τ, was applied. During this period, the xy-components of the magnetization vector, M_{xy}, were dephasing because of spin–spin interaction and, in the meantime, all x-, y-, and z-gradient coils were turned on for phase encoding. At the end of τ, the gradient coil was turned off and a period of D_{10} is required to stabilize the field. A pulse of a few hundred microseconds, D_7, was applied after stabilization for the T_2-weighting as the spin continued dephasing. This same T_2-weighting period of D_7 is required for detection of the echo signal after a $(\pi)_x$ pulse is applied to rotate the dephased M_{xy} components from the $+y$ to the $-y$ axis. The receiver was turned on for a period of AQ for detection of the echo. A negative echo signal was recorded, that is, the echo occurred at the negative y-axis. Finally, a long D_0 lets the excited nuclei release their energy through spin-lattice relaxation in preparation for a new cycle starting with a $(\pi/2)_{-x}$ excitation for recording of a positive echo signal. These negative-echo and positive-echo measurements will minimize the error resulting from the inaccuracy of the parameters such as the r.f. pulse width. Fig. 2 shows an example of the ^{1}H nuclear spin echo signal detected from the binder in the alumina green compacts. Once this second cycle is finished, the strength of phase encoding was stepped up by incrementally increasing $M1$ and $M2$ values. In

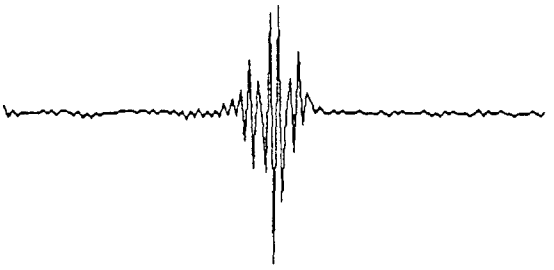

Figure 2 ^{1}H nuclear spin echo signal detected from the binder of an alumina green compact bonded with paraffin wax, polypropylene, and stearic acid.

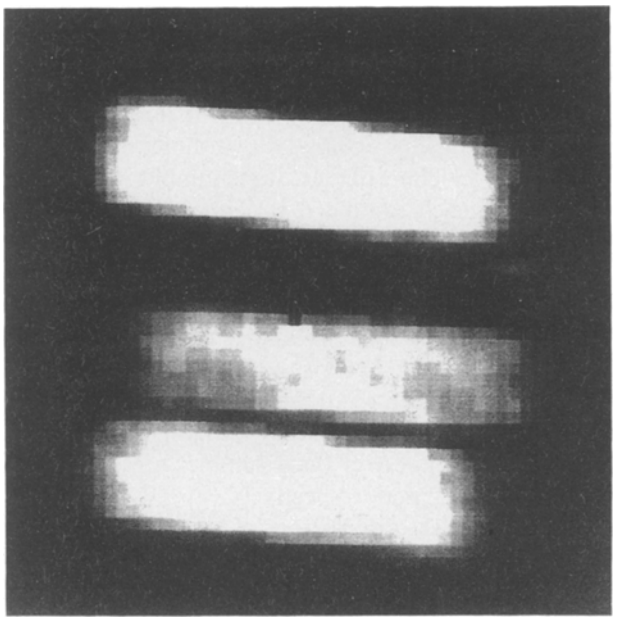

Figure 3 Two-dimensional NMR (xy-plane) imaging shows that the top sample has the highest binder concentration while the middle sample has the lowest. Images represent integrated concentrations through specimen thickness. A spacer was used between top and middle sample so that the orientation of the picture can be identified.

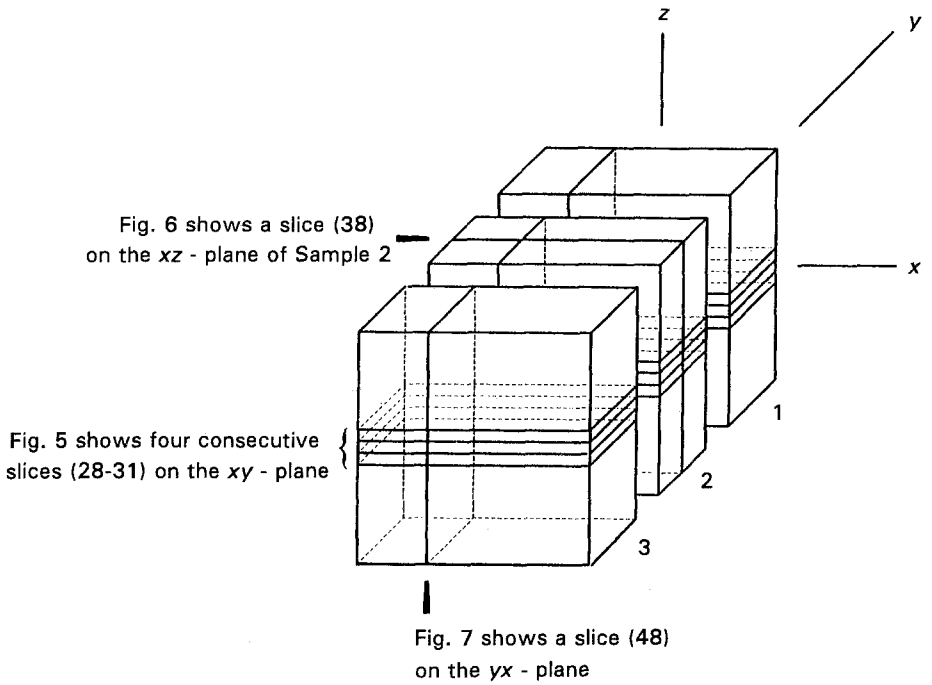

Figure 4 Schematic illustration of three-dimensional orientations of slices shown in Figs 5–7.

our experiment, 64 increments were applied along each y- or z- gradient to obtain a $64 \times 64 \times 64$-sliced mapping on xy-, xz-, and yz-plane for each specimen. A total of 192 pictures was examined. In this sequence, the second Hahn's delay used in T_2 detection [24, 25] is included in the AQ pulse. In order to detect the echo at the centre of AQ, $\tau = (AQ - D_1)/2$ is required. The echo time, TE, starting from the end of the 90° pulse, is $AQ + 2(D_{10} + D_7) + D_2 + 3St$, where D_1 and D_2 are the 90° and 180° pulse width, respectively, and St is the time required for switching-on (or off) the gradient coils.

In acquiring a two-dimensional imaging, the dimension of the z-axis will be set to 1, and $M2$ (field gradient multiplier) in Fig. 1 set to 0 for an xy-plane image. An xz-plane two-dimensional mapping can also be obtained by setting $M1 = 0$ and the y-axis dimension to 1. Fig. 3 shows a two-dimensional mapping on the xy-plane of these three samples. The image intensity in each sample represents its nuclear echo intensity from the binder and thus indicates its binder content if no other factors affecting the echo intensity occurred. Clearly, a comparison in their relative intensities indicates that the binder content in the top sample (Sample 1 in [24]) is the highest and the middle sample (Sample 2 in [24]) the lowest. This agrees very well with our previous study [24]. Note that the length and thickness of these samples are approximately 13 and 3.2 mm, respectively.

Fig. 4 shows the orientations of slices to be shown in Figs 5–7. Each of these orientations indicates a specific part of the samples to be examined in these figures. Fig. 5 shows four consecutive slices (slice 28–31) from the xy-plane. It shows a varying degree of binder inhomogeneity in each of the three samples, especially in the middle sample. A dark spot means a spot with a low binder concentration which can either be a void or an alumina agglomerate. These four consecutive slices are separated by approximately 0.23 mm from each other. The middle sample appears to be the most inhomogeneous and in some point, the binder "folding lines" of high binder concentration can be observed from the yz-plane (Fig. 6, slice 38 on the xz-plane). These folding lines were probably formed due to the inadequate mixing of the alumina powders and the binder. Because these compacts were fabri-

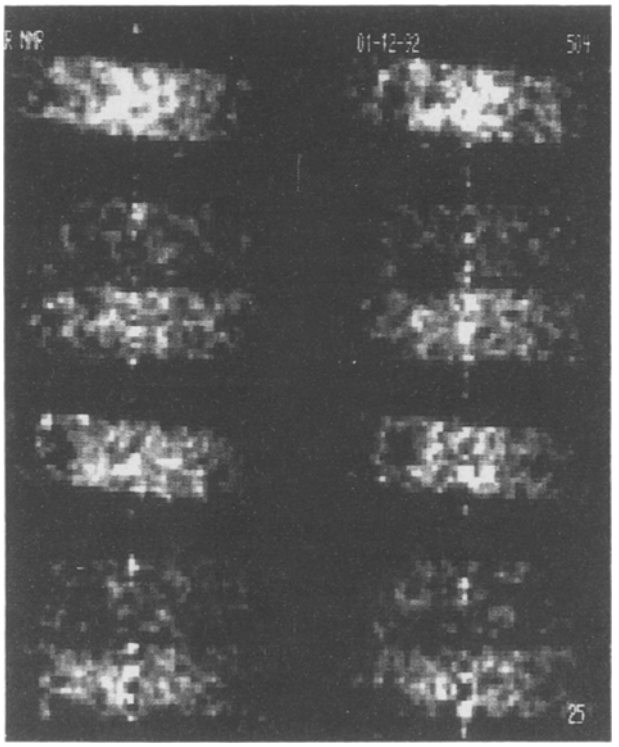

Figure 5 Three-dimensional NMR imaging showing inhomogeneity of binder; a dark spot represents low binder region. The picture shows four consecutive internal slices (on the xy-plane), 0.23 mm apart (slices 28–31). The slice order is 28, 29, 30, 31.

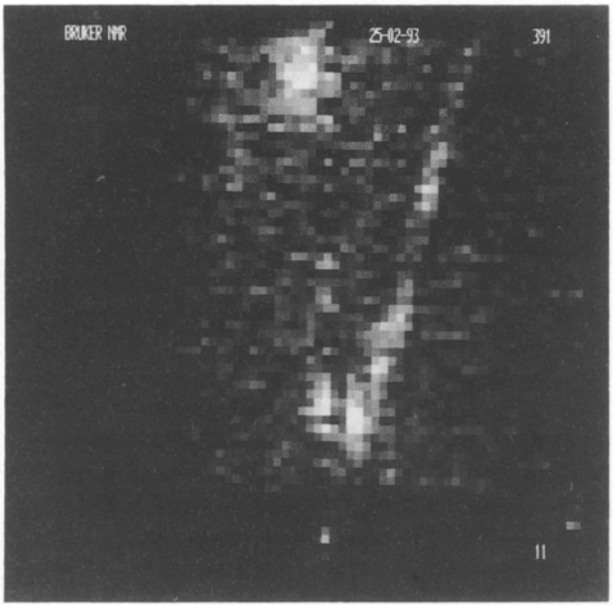

Figure 6 An *xz*-plane slice in Sample 2 (slice 37) indicates a "folding line" of rich binder area. The strips of white areas represent binder-rich regions.

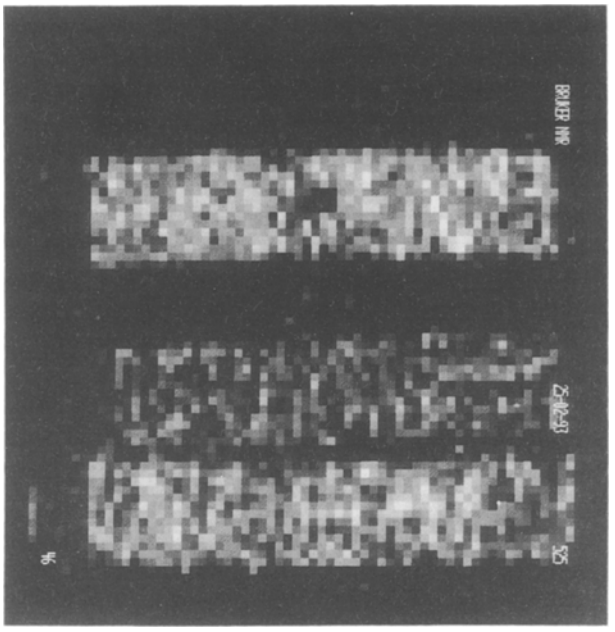

Figure 7 A *yz*-plane slice (slice 48) showing a low binder spot detected at the centre of the sample with highest binder content (top of the picture). The middle sample still shows the lowest binder content.

cated specifically to investigate binder inhomogeneity by NMR imaging, they do not reflect the state-of-the-art of injection-moulding technology. Binder segregation can be observed even in the compact with the highest binder concentration. At the top of Fig. 7 (slice 48 of the *yz*-plane), a low binder region was detected at the centre sample 1 which has the highest binder content of the three samples. In injection moulding, temperature homogeneity of the melt is one of the important factors influencing the binder homogeneity. In the case of the mould temperature being lower than that of the melt, the portion of the melt in contact with the mould may have higher viscosity than that in the centre. This can result in a moulded part having a different density in the centre from its surroundings. This may be the reason for the formation of a low binder region in the top sample in Fig. 7.

4. Conclusion

NMR imaging is a versatile technique for advanced ceramic materials characterization. The current primary technical barrier in the application of NMR imaging to ceramic materials science is the line-broadening due to nuclear dipole–dipole interaction in solids. Application of nuclear T_2-weighted imaging at proton frequency in injection-moulded alumina green compacts containing polypropylene, wax, and stearic acid as binders clearly demonstrated versatility of NMR imaging. Some highly relevant information, such as binder content, internal binder distribution, and density homogeneity, was obtained. Three-dimensional images by the phase-encoded and T_2-weighted nuclear spin echo techniques demonstrated the ability of NMR to detect internal structural imperfections in these green compacts.

Acknowledgements

The authors thank Professor R. M. German, Department of Engineering Science and Mechanics, Pennsylvania State University, for his advise and suggestions on injection-moulding technology. Interesting discussions with Dr Robert Taylor and Dr Samuel Gravina, Bruker Instruments, are also appreciated.

References

1. R. M. GERMAN, K. F. HENS and S. T. P. LIN, *Ceram. Bull.* **70** (1991) 1294.
2. J. A. MANGELS and W. TRELA, in "Advances in Ceramics", Vol. 9, edited by J. Mangels, (American Ceramic Society, Columbus, OH, 1984) p. 220.
3. B. C. MUTSUDDY, *Proc. Br. Ceram. Soc.* **33** (1983) 117.
4. K. H. SWEENEY and R. D. GECKLER, *J. Appl. Phys.* **25** (1954) 1135.
5. A. JOHNSON, E. CARLSTROM, L. HERMANSSON and R. CARLSSON, *Proc. Br. Ceram. Soc.* **33** (1983) 139.
6. A. M. LITMAN, N. R. SCHOTT and S. W. TOZLOWSKI, *Soc. Plas. Eng. Technol.* **22** (1976) 549.
7. F. F. LANGE, *J. Am. Ceram. Soc.* **66** (1983) 393.
8. B. KELLET and F. F. LANGE, *ibid.* **67** (1984) 369.
9. F. F. LANGE and F. METCALF, *ibid.* **66** (1983) 398.
10. F. F. LANGE, B. E. DAVIS and I. A. AKSAY, *ibid.* **66** (1983) 407.
11. I. PELTSMAN and M. PELTSMAN, *Interceram.* **4** (1984) 56.
12. J. A. MANGELS, *Ceram. Eng. Sci. Proc.* **3** (1982) 529.
13. I. I. RUBIN, "Injection Moulding Theory and Practice" (Wiley, New York, 1972) pp. 270–317.
14. A. JOHNSSON, E. CARLSTROM, L. HERMANSSON and R. CARLSSON, *Proc. Br. Ceram. Soc.* **33** (1983) 139.
15. J. L. ACKERMAN, W. A. ELLINGSON, J. A. KOUTCHER and B. R. ROSEN, "Nondestructive Characterization of Materials II" (Plenum Press, New York, 1987) p. 129.
16. W. A. ELLINGSON, J. L. ACKERMAN, L. GARRIDO, J. D. WEYAND and R. A. DIMILIA, *Ceram. Eng. Sci. Proc.* **8** (1987) 503.
17. J. L. ACKERMAN, L. GARRIDO, W. A. ELLINGSON and J. D. WEYAND, "Nondestructive Testing of High-Performance Ceramics" (American Ceramic Society, Columbus, OH, 1988) p. 88.

18. K. HAYASHI, K. KAWASHIMA, K. ROSE and T. INOUYE, *J. Phys. D Appl. Phys.* **21** (1988) 1037.
19. L. GARRIDO, J. L. ACKERMAN, W. A. ELLINGSON and J. D. WEYAND, *Ceram. Eng. Sci. Proc.* **9** (1988) 1465.
20. W. A. ELLINGSON, P. S. WONG, S. L. DIECKMAN, J. P. POLLINGER, H. YEH and M. W. VANNER, *ibid.* **10** (1989) 1022.
21. W. A. ELLINGSON, P. S. WONG, S. L. DIECKMAN and J. L. ACKERMAN, *Am. Ceram. Soc. Bull.* **68** (1989) 1180.
22. L. GARRIDO, J. L. ACKERMAN and W. A. ELLINGSON, *J. Mag. Reson.* **88** (1990) 340.
23. P. S. WANG, D. B. MINOR and S. G. MALGHAN, *J. Mat. Sci.* **28** (1993) 4940.
24. P. S. WANG, S. G. MALGHAN, S. J. DAPKUNAS, K. F. HENS and R. RAMAN, *ibid.* **29** (1994).
25. E. L. HAHN, *Phys. Rev.* **80** (1950) 580.
26. H. Y. CARR and E. M. PURCELL, *ibid.* **94** (1954) 630.

Received 25 June
and accepted 10 December 1993